Report on Aluminum and Inelastic Backgrounds

Submitted to
US Department of Energy Office of Science
Nuclear Physics Division

by the MOLLER Collaboration

at the Thomas Jefferson National Accelerator Facility

December 1, 2015

1 Overview

1.1 Introduction

The MOLLER experiment [1] has been proposed to carry out an ultraprecise measurement of the parity-violating left-right asymmetry in the scattering of longitudinally polarized 11 GeV electrons off electrons in a liquid hydrogen target in Hall A at Jefferson Laboratory (JLab). A successful measurement would provide unprecedented sensitivity to physics beyond the Standard Model, particularly purely leptonic contact interactions beyond the reach of existing high energy colliders, as well as to 100 MeV-scale dark photons that might have small mixing with the Z^0 boson. It would achieve the most precise determination of the weak mixing angle at low energy, comparable in uncertainty to the best ever single measurement at high energy colliders, and best such uncertainty among potential new measurements being proposed or planned in the next decade, either at colliders or at low energy.

The JLab Program Advisory Committee gave MOLLER an A rating, and recommended the allocation of the full beamtime request of 344 PAC days. In September 2014, the Office of Nuclear Physics at the Department of Energy carried out a Science Review of MOLLER. The presentations to the committee and the resulting report and excerpts of comments from panelists can be found here [2]. There were two recommendations in the report, one addressing backgrounds and the other addressing the theory prediction. This report is in response to the background recommendation. Specifically, the background recommendation requested that "further studies of inelastic e-p and e-Al backgrounds should be reviewed and a report submitted to the Office of Nuclear Physics by December 3, 2015".

In the next subsection, we provide a brief summary of the principal backgrounds, the approach taken in the design of the apparatus to reduce backgrounds and maintain the ability to make small and robust corrections, and our analysis approach to measure the principal components of the irreducible electron background. This is followed by a description of the salient features of the apparatus that are relevant to understand the distribution of signal and backgrounds at the detectors. We then describe the characteristics of the target window and inelastic backgrounds in detail and our estimates for the size of the backgrounds and the systematic errors in the corrections. Before summarizing, we briefly discuss our estimates for other backgrounds and our ongoing activities on optimizing the design of the apparatus to reduce systematic errors.

1.2 Backgrounds

The MOLLER apparatus is designed to:

- produce a large flux of Møller electrons from a 75 μA 11 GeV longitudinally polarized electron beam incident on a liquid hydrogen target

- collimate the relevant range of laboratory scattering angles (6 to 17 mrad corresponding to Møller electrons between 3 to 8 GeV) in the full range of the azimuth

- direct the selected Møller electrons to a region otherwise free of background so that the scattered flux can be integrated to measure the parity-violating asymmetry.

The Møller signal is fashioned into a "peak" in the radial direction by the spectrometer at the detector plane approximately 30 m downstream of the target. The primary Møller detectors must measure the flux that traverses a relatively thin annular ring (width ~ 5 cm) of approximately 95 cm radius. A ring of 84 quartz tiles covering this ring form the primary Møller detectors. The Cherenkov light from the quartz is directed radially outwards by air lightguides onto photomultiplier tubes (PMTs) that are enclosed in shielding in an annulus that is approximately 1.5 m in radius.

The background at the PMTs can be broken into three broad categories:

1. Irredudicible electrons that originate from beam electrons (and associated bremßtrahlung) scattering off target material other than target electrons: specifically protons and Al nuclei in the target windows

2. Cherenkov light generated by other charged and neutral particles impinging on the detector quartz

3. Light and charged particles generated in the lightguides by electrons and other background radiation.

The dominant background components are from the first category, which is the focus of this report. It is noted that pre-R&D and simulations are under way to improve our estimates and systematic errors from the subdominant second and third categories as well.

1.2.1 Design Strategy

A complete conceptual design of the MOLLER apparatus has been developed and the important features relevant to gaining an understanding of the irreducible electron background will be discussed in the next section. There are six overall constraints that have driven the optimization of the current design:

1. The overall apparatus must be no more than 30 m long (excluding beam monitoring instrumentation)

2. The primary toroids must be made of water-cooled copper windings (no superconductors)

3. The area traversed by the signal Møller electrons at the detector plane is minimized

4. 100% azimuthal acceptance

5. Two-bounce collimation from target to quartz in the Møller ring i.e. photons generated at the target cannot reach the detectors directly or with just one reflection

6. Instrumenting a sufficiently wide annulus at the detector plane, with significant radial and azimuthal segmentation, to measure variations of fluxes as well as parity-violating asymmetries.

While the first five criteria determine the geometry and parameters of the target, collimator and spectrometer, it is the sixth criterion that allows us to unfold the various background components and facilitates a robust background subtraction. In particular, the poorly known and difficult to calculate behaviour of the inelastic electron-proton weak neutral current vector coupling as a function of inelasticity will be directly measured in auxiliary quartz detectors adjacent to the main Møller ring.

1.2.2 Analysis Strategy

As alluded to above and to be described in the next section in detail, the parity-violating asymmetries in the scattered electron flux will be monitored in 18 different categories of tiles depending on its relative placement at the detector plane as a function of the radial distance from the beamline, and its azimuthal orientation with respect to the mid-planes of the spectrometer azimuthal sectors. There are large variations in the rates and parity-violating asymmetries in these tiles depending on the relative contributions from Møller, elastic e-p, inelastic e-p and elastic e-Al scattering.

Our approach, as will be described at the beginning of Sec. 3, is to analyze these measured asymmetries by two different albeit related methods, after first subtracting out asymmetry and dilution components which are smaller or comparable to the ultimate statistical error i.e. of the order of 3% or less. These will include all subdominant components (second and third background categories in the PMTs described above). The first method is to carry out a simultaneous fit of the remaining components using dilutions determined from Monte Carlo simulations and extract independent parity-violating couplings for the chosen $e - X$ scattering processes.

Using the measured couplings in method 1, the second method will treat the Møller ring detector raw asymmetries as the primary measurements and then carry out a background subtraction using the Monte Carlo dilutions and the parity-violating couplings extracted from the data in the first step. This will be described in detail in the following. It should be noted that there will be significant cross-checks of our modeling of the rate contributions from all the sources as a function of radius from a series of systematic checks via tracking detector measurements at the nominal spectrometer settings, a scan of the spectrometer current, and special runs with a "sieve-slit" collimator that would select much narrower laboratory scattering angle ranges.
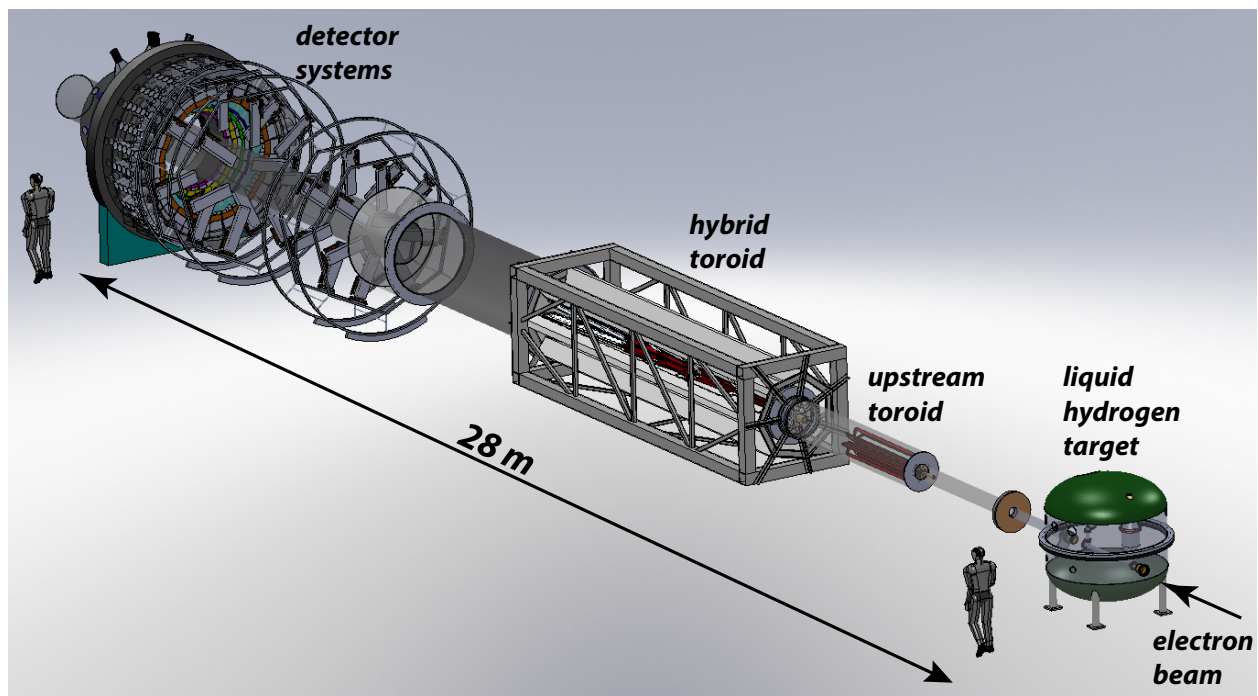
2 Experimental Overview

Figure 1: *MOLLER experiment layout of the target, spectrometer and detectors.*

This section provides a brief overview of the MOLLER experimental design with an emphasis on those aspects that are most critical for separating the Møller electron signal from the irreducible backgrounds mentioned in the introduction. An overview of the main components of the MOLLER experiment layout is shown in Fig. 1.

The measurement would be carried out in Hall A at Jefferson Laboratory, where a nominally 60 μA, 11 GeV, 90% longitudinally polarized electron beam would be incident on a 1.5 m liquid hydrogen target with 100 μm thick aluminum entrance and exit windows. Møller electrons (beam electrons scattering off target electrons) in the full range of the azimuth and spanning the polar angular range 5 mrad $< \theta_{lab} <$ 17 mrad, would be separated from background and brought to a ring focus $\sim$ 30 m downstream of the target by a spectrometer system consisting of a pair of toroidal magnet assemblies and precision collimators.

The Møller ring would be intercepted by a system of quartz detectors; the resulting Cherenkov light would provide a relative measure of the scattered flux. Auxiliary quartz detectors in the focal plane adjacent to the main Møller ring provide the additional information needed for robust backgrond subtraction. A

Table 1: *Nominal design parameters for the proposed MOLLER apparatus. Note that some of the design parameters will change at the few percent level as the design is further optimized. The anticipated beam current is 60 μA, but the apparatus will be designed to operate up to 85 μA, which is assumed for rate related quantities in this table.*

Parameter	Value
E [GeV]	≈ 11.0
E' [GeV]	1.7 - 8.5
θ_{cm}	46°-127°
θ_{lab}	0.23°-1.1°
$< Q^2 >$ [GeV^2]	0.0058
Maximum Current [μA]	85
Target Length (cm)	150
ρ_{tgt} [g/cm^3] (T= 20K, P = 35 psia)	0.0715
Max. Luminosity [cm^{-2} sec^{-1}]	$3.4 \cdot 10^{39}$
σ [μBarn]	≈ 40
Møller Rate [GHz]	≈ 140
ΔA_{raw} [ppb]	≈ 0.6
$< A_{pv} >$ [ppb]	≈ 35
$\Delta A_{stat}/ < A_{expt} >$	2.0%

pion detector located behind the main Møller ring will measure both the asymmetry and rate from the small ($\sim 0.1\%$) contamination from pions and other charged hadrons. Periodically, a tracking system operating at much lower beam current will be inserted to provide a fine-grained measurement of the focal plane spatial rate profile for comparison to simulation. Some key design parameters of the proposed apparatus are summarized in Table 1.

We now describe the critical elements of the system for the separation of the Møller signal and the irreducible backgrounds. The primary acceptance defining collimator is located just upstream of the upstream toroid in Fig. 1. The seven open slots in the collimator ("septants") cover a symmetric range of $60° \lesssim \theta_{COM} \lesssim 120°$ about 90° in COM scattering angle, corresponding to extremely forward angles in the range 6-17 mrad in the highly boosted laboratory frame. The Møller electrons that pass the primary acceptance collimator correspond to a scattered electron energy range of 2.75 - 8.25 GeV.

The primary challenge of the spectrometer design is to achieve a focus for this broad momentum range, while providing good separation in the focal plane from the primary background of electrons from elastic and inelastic e-p and e-Al scattering. As shown in Figure 2, this goal has been achieved by a novel system consisting of two toroidal magnets. The broad momentum range of Møller electrons is focussed ~ 30 meters downstream of the target while maintaining a good separation from the somewhat de-focussed e-p elastic peak.

Full focal plane and radial scattered electron distributions for a focal plane chosen 28.5 meters downstream of the target are shown in Fig. 3 and Fig. 4. The radial region from 0.7 - 1.2 meters from the beam centerline will be divided into six concentric rings of detectors. The Møller events dominate ring 5, while the backgrounds from elastic and inelastic e-p and e-Al scattering play a more important role in other rings. The azimuthal distribution in Fig. 3 also displays a distinct pattern that is different between the signal Møller events and background processes such as elastic e-p events.

To take full advantange of the signal/background discriminating power of the radial and azimuthal distri-
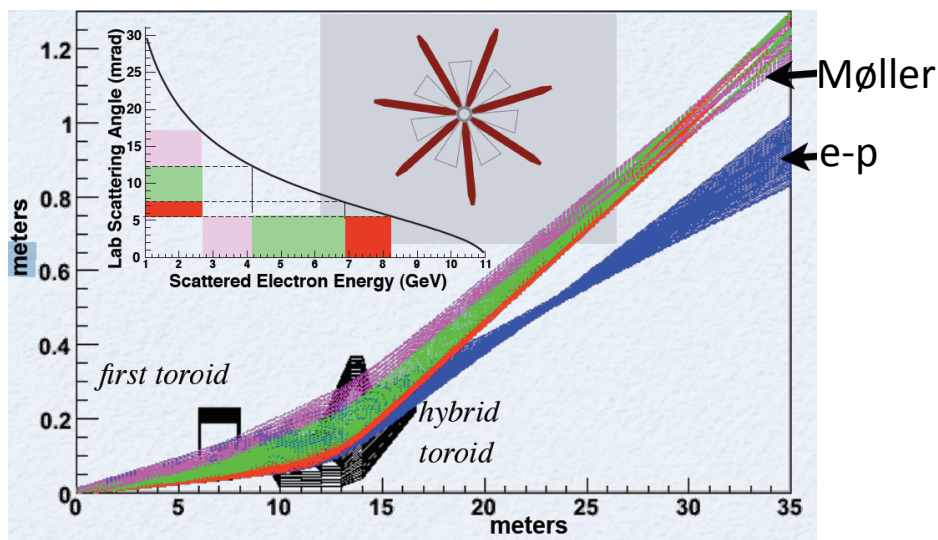
Figure 2: *Basic focussing properties of the two toroid spectometer system illustrated with low, medum, and high energy Møller scattered electrons and elastic e-p electrons.*
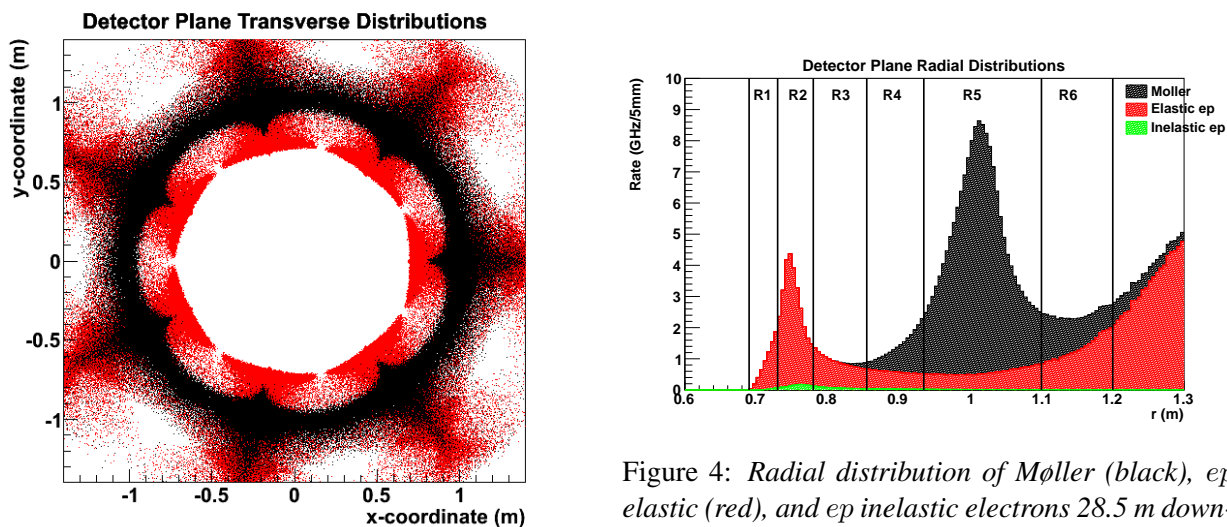

Figure 3: *Full focal plane distribution of Møller (black) and ep (red) electrons 28.5 m downstream of target*

Figure 4: *Radial distribution of Møller (black), ep elastic (red), and ep inelastic electrons 28.5 m downstream of target. The vertical black lines delineate the proposed radial segmentation into 6 rings (R1 thru R6). The principal A_{PV} measurement will be carried out in ring R5.*

butions, the focal plane detectors have significant radial and azimuthal segmentation. The full, cross-section weighted focal plane distribution is shown in Fig. 5, while Fig. 6 shows one toroidal sector with the antici-pated radial and azimuthal segmentation of the quartz tiles. There are six radial rings, with each azimuthal septant sector sub-divided into 4 sub-sectors, resulting in a total of 28 azimuthal channels at each radial bin. The exception to this is the Møller radial bin (ring 5), which has each azimuthal channel further sub-divided into three additional bins for a total of 84 channels. The total number of detector tiles in the focal plane

is 224. For the purposes of this report, we categorize these tiles into 18 different types that we use in the background unfolding procedure described in the next section. Each sector has six radial rings with three types of azimuthal tiles: **open** (red), **closed** (blue), and **transition** (green), where the colors correspond to the code in Fig. 6. Open detectors are located in the center of the azimuthal sectors defined by primary collimator openings, with closed detectors in the center of the blocked azimuthal sectors, and transition detectors straddling the open and closed sectors.
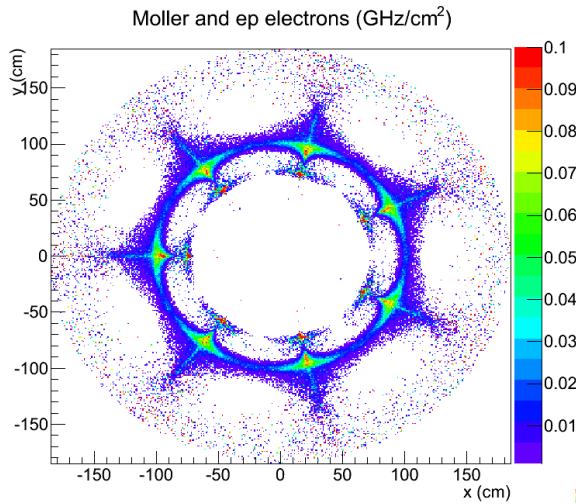

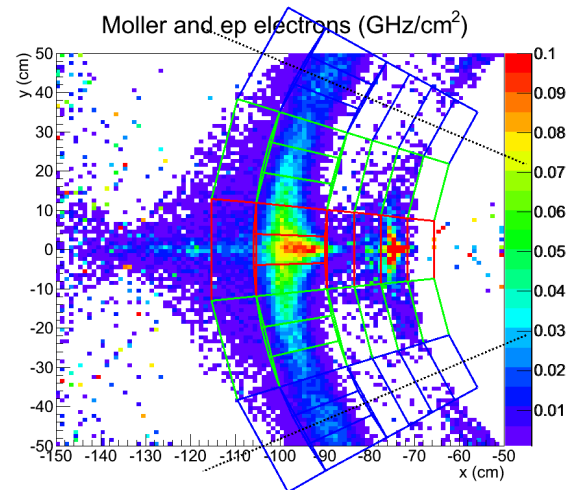Figure 5: *Simulated, cross-section weighted, Møller and ep electron rates.*

Figure 6: *Superimposed azimuthal and radial bins (detector locations) in one toriodal sector (indicated by the dotted black line).*
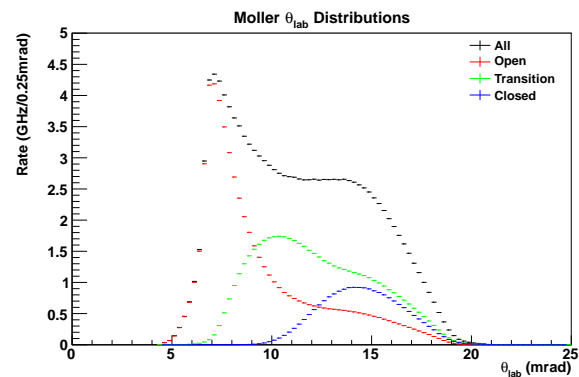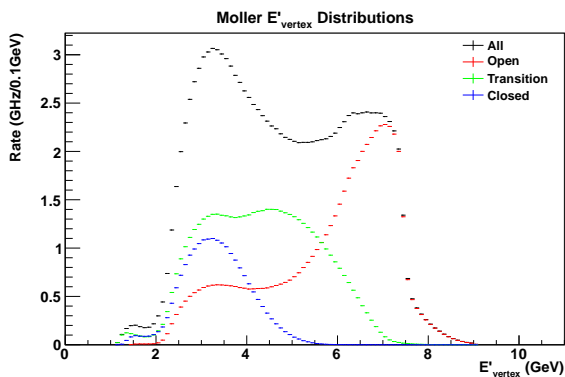

Figure 7: *Rate of Møller electrons as a function of E'_{vert}, the energy of the scattered electron immediately after the interaction (left), and θ_{lab}, the scattering angle in the laboratory frame (right). The detected particles are colored according to which detector they hit, red for the detector in the center of the open sector, blue for the detector in the center of the closed sector and green for the detector which straddles the open and closed sector.*

Both the signal and background processes have an azimuthal signature that helps in discriminating them. An example of that is shown in Fig. 7. In the Møller ring (ring 5), the three different types of azimuthal tiles (open, closed, transition) have very different distributions of scattered electron energy E'_{vert} and the corre-

lated quantity laboratory scattering angle θ_{lab}. This azimuthal "defocussing" effect is due to radial fields in the spectrometer toroidal magnets that have the largest effect for the lowest energy scattered particles. Each of the background processes has its own distrinct azimuthal kinematic separation that affects both the asymmetry and rate, thus providing an important handle in the background unfolding procedure.

3 Aluminum Target Windows

The 150 cm long MOLLER hydrogen target will have ~ 100 μm thick entrance and exit windows made of aluminum. The dilution and asymmetry from electron scattering off Al nuclei represents one of the irreducible background corrections. The aluminum end window correction in the Qweak experiment [4] led to a $\sim$28% correction to the parity-violating e-p asymmetry that Qweak measured. The correction for the MOLLER experiment will be much smaller (about 1.5%). Below, we briefly describe the Qweak correction and provide a simplified estimate of why it will be significantly smaller in MOLLER before moving on to the detailed simulations in Sec 4.1.
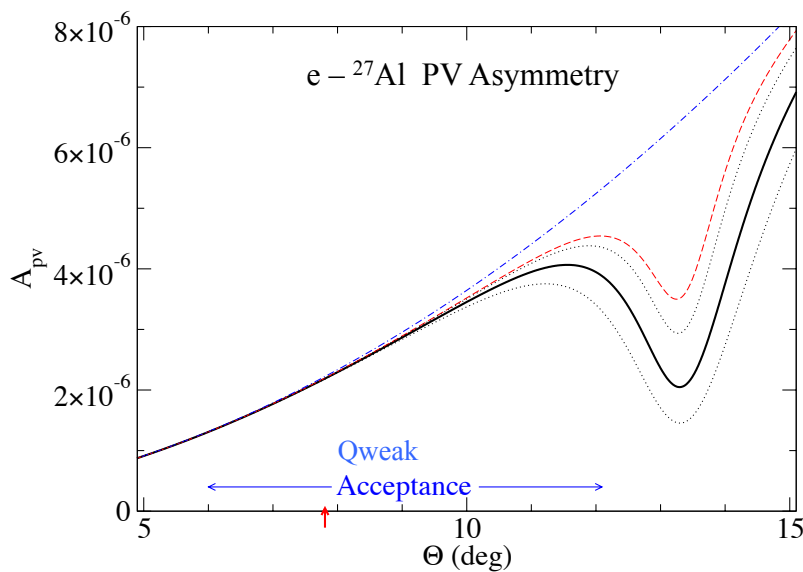
3.1 Qweak vs MOLLER

Figure 8: *Parity-violating asymmetry prediction, vs. lab scattering angle, for elastic scattering of 1160 MeV electrons from* ^{27}*Al from C. Horowitz [3]. The blue dot-dashed curve shows plane wave Born approximation results, while the other curves show distorted wave results under various assumptions. The average momentum transfer of the Qweak experiment is shown by the red arrow, while the angular acceptance is very roughly indicated by the blue arrow range.*

For the kinematics of the Qweak experiment (E = 1155 MeV, $\theta_{lab} \sim 7.9°$, $Q^2 = 0.025$ (Gev/$c)^2$), the contribution of the aluminum windows to the rate is about $\sim$ 3.2% (about 76% of which is e-Al elastic nuclear scattering). A detailed calculation of the e-^{27}Al parity-violating asymmetry has been performed by Horowitz [3] as shown in Fig. 8. At the average momentum transfer of the Qweak experiment (indicated by the red arrow in the figure), the asymmetry is $\sim$2200 ppb, significantly larger than the e-p asymmetry of

~ -240 ppb. The reason for the difference is easy to understand from the Born approximation expression for the asymmetry:

$$A_{PV}(_Z^N X) = -\frac{Q^2 G_F}{4\pi\alpha\sqrt{2}}\left[Q_W^p + \left(\frac{N}{Z}\right) Q_W^n\right] \tag{1}$$

The aluminum asymmetry is dominated by the weak charge of the neutron. Numerically (with $Q_W^p(\text{SM}) = 0.0710$ and $Q_W^n(\text{SM}) = -0.9878$), the ratio of the e-^{27}Al and e-p PV asymmetries is ~ 14. So, despite the relatively small rate contribution of 3.2%, the $2200/240 = 9$ times larger asymmetry leads to a 28% contribution to the measured asymmetry in the Qweak experiment. Qweak ultimately anticipates knowing this correction to better than 10% of itself.

This contribution will be significantly smaller in the MOLLER experiment for two main reasons. The ratio of aluminum to hydrogen is about a factor of four ($35/150$, the ratio of hydrogen target lengths) smaller in the MOLLER experiment. Most importantly, in Qweak the full elastic e-Al peak was detected along with the e-p elastic peak. In contrast, for MOLLER, the e-Al elastic peak is well separated spatially from the main Møller peak (see Fig.11 in Section 4.1). It is only its radiative tail (about 12% of the peak rate) that gets detected. There are some other less significant factors that must be taken into account in comparing Qweak to MOLLER.
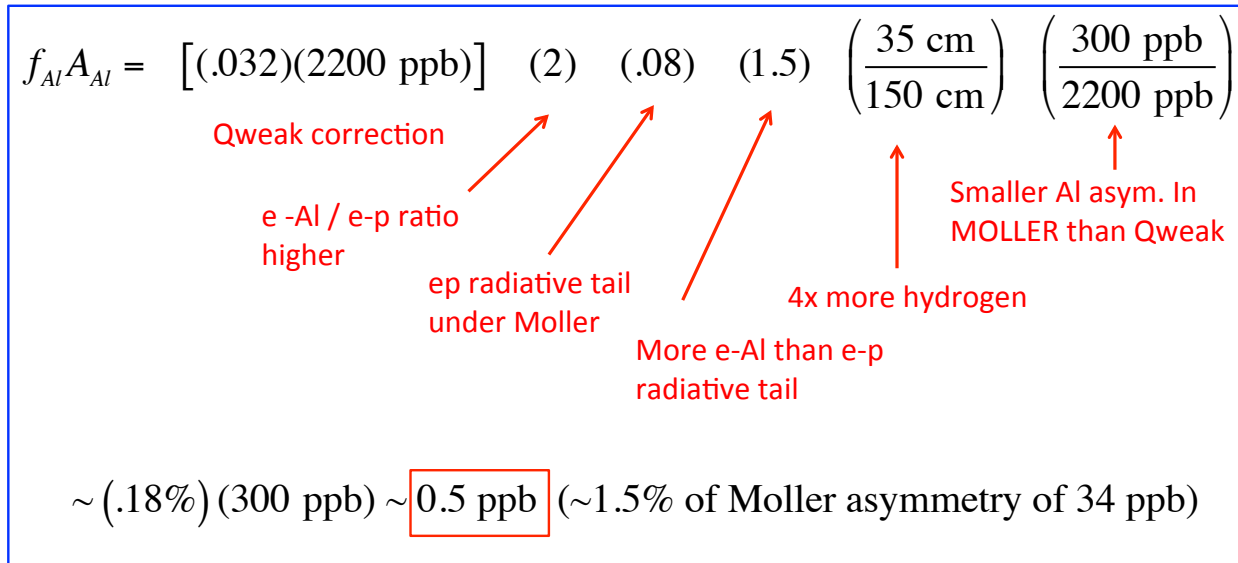

$$f_{Al}A_{Al} = \left[(.032)(2200 \text{ ppb})\right] \quad (2) \quad (.08) \quad (1.5) \quad \left(\frac{35 \text{ cm}}{150 \text{ cm}}\right) \quad \left(\frac{300 \text{ ppb}}{2200 \text{ ppb}}\right)$$

Qweak correction

e -Al / e-p ratio higher

ep radiative tail under Moller

More e-Al than e-p radiative tail

4x more hydrogen

Smaller Al asym. In MOLLER than Qweak

$$\sim (.18\%)(300 \text{ ppb}) \sim \boxed{0.5 \text{ ppb}} (\sim 1.5\% \text{ of Moller asymmetry of 34 ppb})$$

Figure 9: *Extrapolation from Qweak Al correction to expected MOLLER Al correction.*

All the various factors that relate the Qweak correction to the MOLLER correction are broken out in Fig. 9 and itemized below:

- e-Al/e-p ratio higher: The Al form factor changes more rapidly than the proton form factor resulting in $\sim$ two times greater contribution from e-Al compared to e-p at the lower Q^2 of MOLLER.

- ep radiative tail under elastic: The fraction of the e-p elastic radiative tail in the Møller ring is $\sim 8\%$

- More e-Al than e-p radiative tail: The fraction of the e-Al radiative tail under the Møller peak is about 1.5 times that of the e-p elastic radiative tail.

- 4x more hydrogen: The Al end windows in the two experiments are the same thickness, but MOLLER has four times as much hydrogen.

- Smaller Al asymmetry in MOLLER than Qweak: Due to the smaller Q^2, the expected e-Al asymmetry in MOLLER is smaller.

The above discussion provides intuition that the correction is about 0.5 ppb, which is 1.5% of the anticipated Møller asymmetry of $\sim$34 ppb. A simulation-based estimate of the correction will be discussed in the next section.

3.2 Theoretical Assumptions

We now briefly describe the assumptions we make in our simulations about the physics processes associated with scattering from the aluminum end windows.

3.2.1 Elastic Scattering

As shown in more detail in the next section, the dominant process from aluminum is the radiative tail of the elastic e-^{27}Al nuclear scattering. For the cross section, we use the aluminum form factor from [9]. The asymmetry can be determined directly from our background fit procedure. As described further in Section 4.4, this results in an asymmetry determination with $\sim$ 30% fractional error. However, this asymmetry can be determined theoretically with much higher precision than this. We note that the accepted Q^2 range of the MOLLER experiment is well below the first diffraction minimum as shown in Figure 10. So the theoretical prediction in a framework like that of Horowitz [3] is considered to be very reliable due to the absence of significant effects due to Coulomb distortions at the MOLLER kinematics and the high precision ($\sim$ 1%) with which the weak charge of the neutron is known. In addition, further confidence will come from an expected Qweak measurement of this asymmetry at a low $Q^2 \sim 0.025$ $(\text{GeV}/c)^2$ with a relative precision of better than 10%. Given these factors, we assign a fractional systematic uncertainty (see section 4.4) of 10% to our correction from e-^{27}Al elastic scattering.
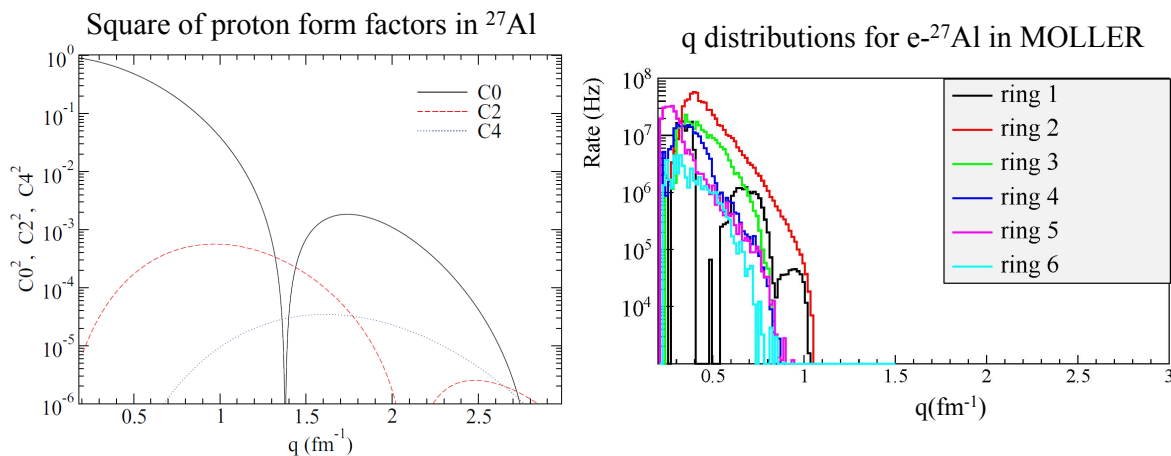
Figure 10: *The square of the significant proton form factor multipoles in e-^{27}Al elastic scattering from Horowitz [3] is shown in the left figure. The lowest diffraction minimum, where Coulomb distortion effects can be important, is at $q \sim 1.4$ fm^{-1}. The right figure shows the q distributions for the e-^{27}Al elastic scattering process in the six detector rings in the MOLLER experiment. All of the accepted q range is well below the first diffraction minimum.*

As noted in the introduction, our analysis strategy involves doing direct subtraction of any background process that is estimated to contribute smaller than the ultimate statistical error (ie. $< 3\%$) to the total asymmetry. For aluminum, the only asymmetry we let float in the fit is the elastic e-^{27}Al asymmetry. For the other processes, we do a direct subtraction before fitting based on the considerations described below.

3.2.2 Quasi-elastic Scattering

For quasi-elastic scattering on ^{27}Al, the empirical fit to electron-nucleus scattering from Bosted and Mamyan [7] is employed. The work uses formulae from Maieron, *et al.* [5] for its quasi-elastic contribution. At MOLLER kinematics the quasi-elastic contribution is small; from simulation we find it to be $\sim 2.3\%$ of the total rate from aluminum. This is smaller than the "naive" expectation of $1/Z = 1/13 = 7.7\%$ that one gets from the ratio of the quasi-static estimate for the total quasi-elastic scattering on the Al nucleus compared to the elastic Al nuclear cross section in the low Q^2 limit where the form factors approach unity. The suppression comes from a Pauli suppression factor assumed in Bosted/Mamyan [7] of $(3/4)(q/k_F)$ which is ~ 0.28 for the MOLLER $q \sim 89$ MeV/c with a Fermi momentum for ^{27}Al of $k_F = 236$ MeV/c.

For the asymmetry, there will be final state interaction and other corrections to the simple quasi-static estimate. These have been considered in Gonzalez-Jimenez *et al.* [8], but they don't present calculations as low as the MOLLER Q^2. For the QE asymmetry on deuterium, Hadjimichael *et al.* [6] did calculations as low as $q = 150$ MeV/c at forward angles and found a factor of three difference between quasi-static and a calculation including final state effects. For the background unfolding procedure presented below, we do a subtraction for quasi-elastic using the quasi-static estimate of its asymmetry. With these assumptions, this results in a $< 0.005\%$ correction to the asymmetry in the detector ring where Møller scattering dominates. With such a small contribution, potential uncertainties of a factor of 3 (300%) on both the cross section and asymmetry still result in a systematic error from this contribution of $< 0.05\%$.

3.2.3 Inelastic Scattering

Contributions to inelastic processes in aluminum include inelastic processes on nucleons in the aluminum nucleus and inelastic excitations of low-lying nuclear excited levels. The former is discussed in the next section. The contribution of the nuclear excited levels has been computed to be $< 3\%$ of the total rate from aluminum for the case of Qweak, and it will likely be smaller in MOLLER due to the larger elastic cross section at lower Q^2. Howowitz [3] argues that only a very modest estimate (of order 50%) of the inelastic level asymmetries is necessary for a situation where the contribution is so small. For this initial background estimate, we have not included any nuclear excited levels. However, we point out that even if we make the conservative assumption that this contribution is as large as for Qweak and it has a 100% fractional uncertainty, this results in a systematic error of $< 0.05\%$ (because it is only 3% of the small 1.5% overall aluminum correction).

3.2.4 Other Nuclides

Finally, there is the presence of impurities in the alloy that is likely to be used for the target windows. The preferred alloy is about 90% ^{27}Al but also contains some Cu, Mg, and Zn and other trace elements. We have not considered these effects here, but Horowitz [3] has argued that the parity-violating asymmetry for these elements can be calculated using relativistic mean field densities. However, we will not need to rely on these calculations directly, because the aluminum asymmetry we measure is dominantly determined by one of the detetor rings where the elastic aluminum peak dominates, so we measure the effective aluminum asymmetry for the real alloy directly and then it is used to determine the radiative tail contribution under the Møller electron peak.

4 Inelastic Scattering at High W
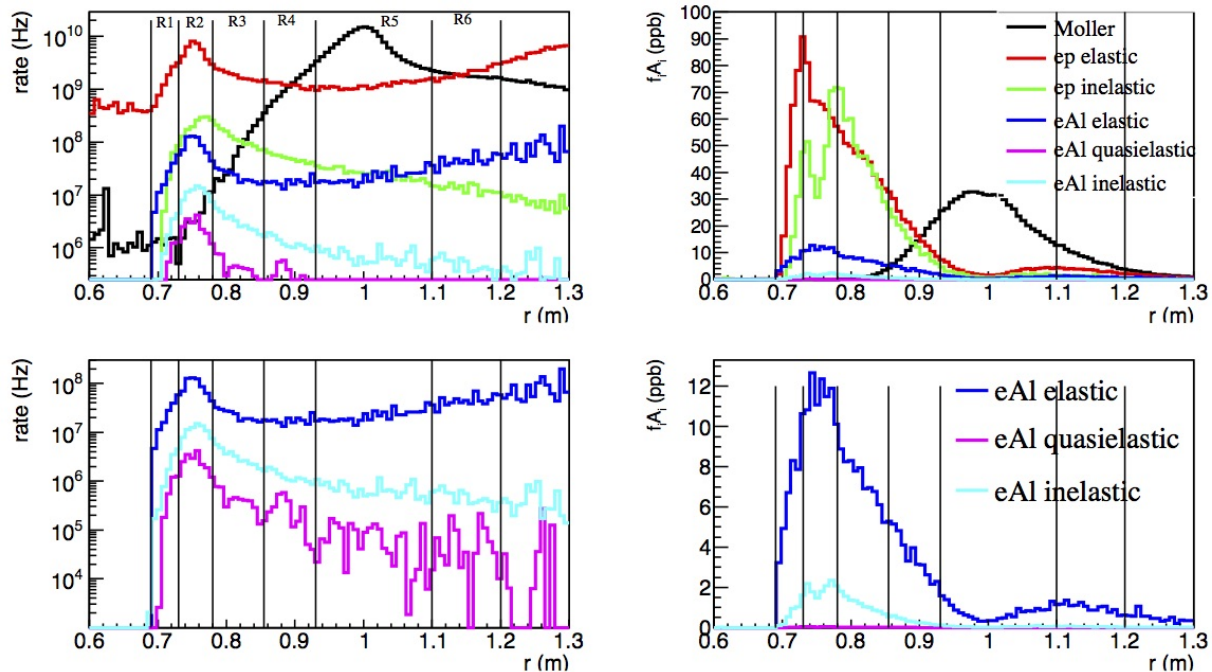
4.1 Simultaneous Fit Strategy

Figure 11: *Simulated signal and background vs. radial location of detected electron at the MOLLER detector ring. In all figures: the Moller electron signal is in black, background from elastic scattering on the proton is red, inelastic scattering from the proton in green, and elastic, quasielastic, and inelastic scattering from the Al target windows in blue, magenta and cyan, respectively. Upper left: rates, in Hz. Lower left: rates for just the Al contributions. Upper right: contribution to the total measured asymmetry, in ppb, for all processes ($f_i A_i$, where f_i is the dilution for the individual process). Lower right: as above, for Al contributions only. Note: the figures on the left have a log scale, while those on the right are linear scale. The boundaries of the 6 detector rings are indicated by vertical black lines.*

Electron distributions at the detector plane are shown in Fig. 11 from a full GEANT 4 [10] simulation of interactions in the long liquid hydrogen target with the approriate collimation and 3-D magnetic field map for the two toroid assemblies. Events were generated in the target from Møller scattering from electrons in hydrogen, elastic and inelastic scattering from protons in hydrogen, and elastic, quasielastic, and inelastic scattering from the Al entrance and exit windows of the target, using appropriate cross sections and material thicknesses. The plots show the detected electron rates *vs.* radial location at the z-location of the MOLLER detector, as well as the dilution-weighted asymmetries $f_i A_i$. The dilution for a given process is defined as

$$f_i = \frac{N_i}{\sum_j N_j},$$

where N_i is the rate of detected events from process i. The rates and asymmetries shown are summed over the full detected azimuth ϕ, and correspond to the maximum beam current of 85 μA and beam polarization of 80%.

These distributions represent what the experiment will see, after we have subtracted out the small backgrounds from particles other than scattered electrons which generate light in the quartz detectors. These small asymmetry and dilution components (the second and third background categories listed in Section 1.2) are each smaller or comparable to our statistical error *i.e.* of the order of 3% or less, and are not discussed further here.

These plots make our strategy clear for dealing with the remaining irreducible backgrounds (*i.e.* from scattered electrons in the detectors from processes other than the Moller-scattering signal). The division of the detector into six radial rings will allow us to measure the asymmetries in rings where the signal completely dominates, *i.e.* ring 5 (0.92 to 1.1 m), where the signal will be about 85% of the measured asymmetry, but also to measure the asymmetries in rings where the various different backgrounds contribute differing fractions to the asymmetry. A simultaneous fit to all these asymmetries, constrained by the various dilution factors for each process, will allow us to extract the Møller asymmetry with high precision, and, along the way, determine the asymmetries of the various background processes as by-products.

Note that these figures actually hide an additional degree of freedom that will be very useful in the fitting process: the azimuthal (ϕ) dependence of the various dilutions and asymmetries. Each detector ring is divided into three ϕ sectors (see Fig. 6). Due to the spectrometer optics, the different ϕ sectors of a given ring will accept a different kinematic range and so each will see different fractions of the various backgrounds. This gives us additional leverage to extract each asymmetry contribution independently, as discussed below.

For this fitting process we clearly need to know (1) the cross sections and kinematics (and thus the dilution f_i) in each detector bin (radius,ϕ) for each process and (2) a model for how the asymmetry A_i varies with kinematics (Q^2 and W) over the detector acceptance (radius,ϕ) bin.

Knowledge of the f_i is not problematic; the relevant form factors and differential cross sections are well-known, so in combination with simulation of the well-determined spectrometer optics we will have the f_i available for each detector element. We can validate these using high-granularity measurements of the total detected electron rates as a function of (radius,ϕ) using our tracking system [1], which will also extract the central kinematics of the experiment. We might even envision using the rate distributions from the tracking system as an additional input constraint to the fitting method.

The expected variation of A_i with kinematics is well-in-hand, of course, for the Møller electrons as well as for e-p elastic scattering, e-Al elastic and e-Al quasielastic scattering. Quasielastic scattering on Al might exhibit significant final-state interaction effects at forward angles; however the total rate for this process is very small, see Fig. 11. At these kinematics, the form factors for inelastic excitation of low-lying nuclear excited states in Al are such that this contribution should be very small as well. The low-lying nuclear excitations are kinematically indistinguishable from the elastic Al events in our spectrometer (E' roughly translates as radius at the detector, and a few 10's of MeV to less than a cm), so they will be subsumed into the e-Al contribution in the fit.

4.2 Inelastic Scattering off Protons

The process of inelastic ep scattering, as well as that same process from the Al target windows, is more challenging. There are only a few data points on the asymmetries for Δ and resonance region production, and none at higher W ([11, 12, 13]). Cross sections are also less well known than for the elastic processes.

The world data on parity-violating asymmetries in inelastic scattering from the nucleon are summarized in Table 2. Note that the data are consistent with a simple scaling: $A_{\text{inel}} = -85 \, \text{ppm}/(\text{GeV})^2 \times Q^2$, without radical W-dependence. One additional datum is from E158 [14], where they extracted the asymmetry from a combination of proton elastic and inelastic scattering, and obtained a result consistent with the standard model proton weak charge and the above scaling at about 20% accuracy. The W-dependence is key for us: the range of accepted Ws for the experiment spans 1 to 5 GeV, and the inelastic background underneath the

Experiment	Q^2	W	A/Q^2
	(GeV^2)	(GeV)	(ppm)
G0 [11]	0.24	1.18	-98 ± 22
PVDIS [12]	0.95	1.26	-72 ± 10
"	0.83	1.59	-89 ± 9
"	0.76	1.86	-82 ± 7
"	1.47	1.98	-81 ± 12
" [13]	1.28	2.03	-61 ± 19
"	1.08	2.07	-84 ± 4
"	1.91	2.33	-84 ± 4

Table 2: World data on parity-violating asymmetries in inelastic scattering from the nucleon.

Møller signal in the main Møller detector ring represents a different mix of W's than the inelastic events measured in the other detector rings. Therefore, if there is a significant variation of the asymmetry with W, then we will need to extract asymmetries for the appropriate regions in W from the simulataneous fit.
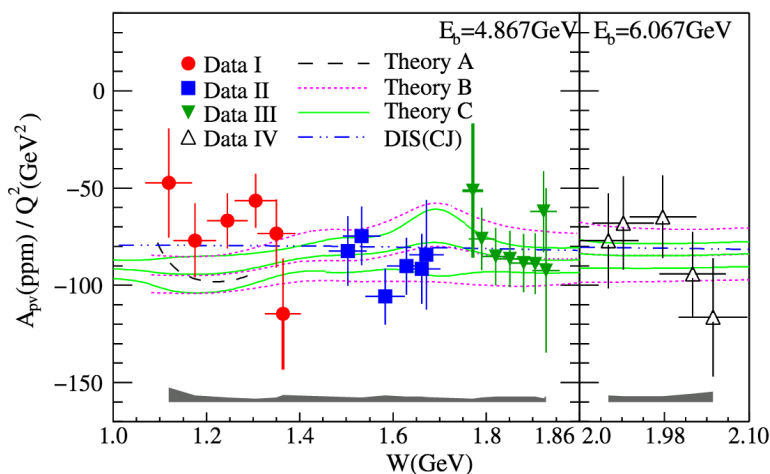

Figure 12: *Inelastic asymmetry from the 6 GeV PVDIS experiment [12] compared to model calculations: Theory A: Matsui et al. [15], Theory B: Gorchtein et al. [16], Theory C: AJM group [17], as well as a duality-based prediction, DIS(CJ).*

Theory does give us some guidance here. Several groups have provided calculations of the inelastic ep asymmetries. These have been mainly motivated by the desire to benchmark calculations of the γZ box diagram contributions for Qweak [20]. Results from Matsui, Sato and Lee [15], Gorchtein, Horowitz and Ramsey-Musolf [16], and the Adelaide-JLab-Manitoba (AJM) collaboration [17] are compared with the 6 GeV PVDIS data in Fig. 12. All the calculations are in good agreement with the data, and suggest at most a modest W evolution in the resonance region. Indeed, the models are in good agreement with the simple $A_{\text{inel}} = -85 \text{ ppm}/(\text{GeV})^2 \times Q^2$ scaling in this W region, at the 20% level.

The AJM group have extended their calculation to the MOLLER kinematic range [18] ($Q^2 \sim 0.004 \, \text{GeV}^2$). The results are shown in Fig. 13. In a more recent publication [21], they have further explored the dependence of the asymmetry on the scale at which they match the high-Q^2 and low-Q^2 region. Assuming a very conservative (100%) uncertainty on the key parameter (the continuum $\gamma - \gamma$ to $\gamma - Z$ rotation parameter)
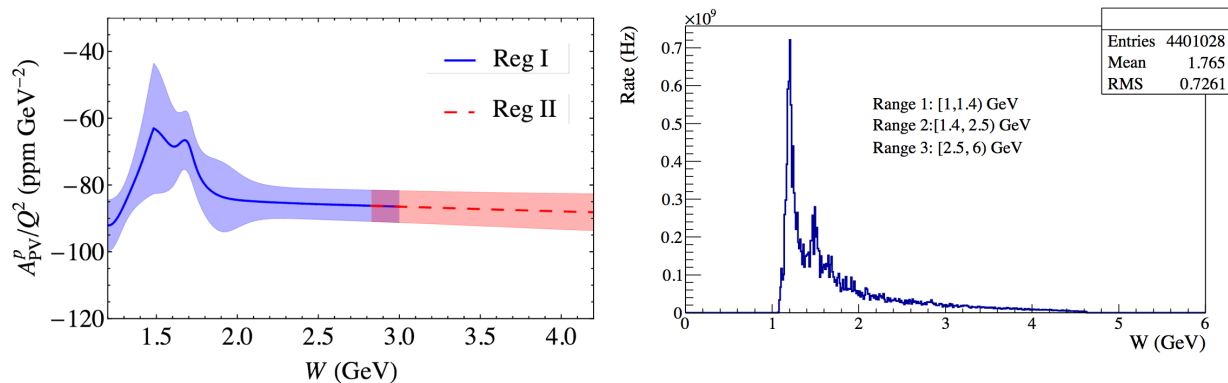
Figure 13: *Left: AJM collaboration [18] calculation of ep inelastic asymmetry for MOLLER kinematics, with theoretical uncertainty band indicated. Right: Simulated rate from ep inelastic scattering vs. W. The ranges for the three bins in W for our asymmetry ansatz are indicated.*

for all $Q^2 < 1 \, \mathrm{GeV}^2$, the relative uncertainty in their Region I kinematics increases from $\sim 8.6\%$ (as shown in Fig. 13) to $\sim 12\%$.

The modest W-dependence shown motivates our ansatz for treating the inelastic asymmetry: we break the kinematics for inelastics into three bins in W: (i) the Δ region, $1 < W < 1.4 \, \mathrm{GeV}$ (ii) the "resonance region", $1.4 < W < 2.5 \, \mathrm{GeV}$, and the "continuum" $2.5 < W < 6 \, \mathrm{GeV}$. We use the Christy-Bosted global fit [19] for the cross sections. Figure 13 shows the simulated rate as a function of W in our acceptance. We then model the inelastic asymmetry in these three bins using $A_{\mathrm{inel}} = K f(W) Q^2$ where K contains electroweak couplings, and $f(W)$ is assumed to be constant in each of the three bins in W. We then treat the three $f(W)$ as free parameters to be extracted from our data via the simultaneous fit to the asymmetries in all bins in (radius, ϕ). We thus minimize uncertainty due to theoretical input on the inelastic asymmetries; we rely *on our data* to extract the inelastic contributions.

We note that we could consider constraining the inelastic asymmetries in certain kinematic regions using existing or future data from other experiments (G_0 [24, 11], PVA4, 6 GeV PVDIS [12], Qweak [20], SOLID), or from available theoretical calculations, but this is not required; in this report, we assume only the use of the MOLLER data itself. We also note that the kinematic distributions of ep-inelastic and e-Al inelastics are essentially indistinguishable in our spectrometer, so the simultaneous fitting procedure will not be able to separate these two contributions.

An additional possible effect may be present in the inelastic asymmetries. Zhu, Maekawa, Holstein and Ramsey-Musolf [23] have studied electroweak radiative corrections at low Q^2 (the photoproduction limit) for inelastic scattering from nucleons, and discovered that the asymmetry contains a contribution from a new low-energy constant in the effective weak Lagrangian, d_Δ which characterizes the parity-violating $\gamma N \Delta$ coupling. This term would lead to a Q^2-*independent* contribution to A_{inel}. Naive dimensional analysis would suggest that this contribution is vanishingly small, however the authors suggest a mechanism for enhancements would could lead to contributions as large as the several ppm scale. An initial search for such a large d_Δ term was conducted by G0 [24]. The results were consistent with no d_Δ contribution, but were not precise enough to rule out a contribution smaller than a few ppm. More precise results on d_Δ will soon be available from Qweak, which should further constrain this effect. In the future, we plan on incorporating an additional Q^2-independent contribution in our ep inelastic asymmetry ansatz in the simultaneous fit; we have not done so yet.

Table 3 shows the total predicted asymmetry in each radial ring, A_m, and its statistical precision σ_A/A

along with the fractional contributions to the measured asymmetries from each relevant process. One can see from this table the strategy of the simultaneous fit. Ring 5 is dominated by the Moller signal. Rings 1 and 2 have very different contributes from ep-elastics and ep-inelastics, allowing these asymmetries to be disentangled. Ring 6 has a large relative contribution from e-Al elastics compared to other rings, *etc.*. Note also that the background fraction from Al elastic scattering in ring 5 is 1.47%, in agreement with the 1.5% scaling estimate from Qweak given above in Fig. 9.

ring #	$\frac{\sigma_A}{A}$ (%)	A_m (ppb)	Møller	e-p elastic	e-p inelastic	e-Al elastic	e-Al quasielastic	e-Al inelastic	pions
			$f_i A_i(\%)$	$f_i A_i(\%)$	$f_i A_i(\%)$	$f_i A_i(\%)$	$f_i A_i(\%)$	$f_i A_i(\%)$	$f_i A_i(\%)$
1	3.05	-78.69	0	79.9	28.6	-9.66	0	1.12	0
2	1.09	-103.1	0	65.3	44.1	-11.3	0	1.83	0.05
3	1.68	-91.15	1.12	50.3	54.3	-8.25	0	1.34	1.13
4	3.06	-44.73	33.5	37.8	28.3	-7.33	0	0.63	7.04
5	1.61	-34.26	88.2	6.61	3.56	-1.47	0	0.09	2.98
6	7.24	-13.28	57.5	25.3	8.40	-7.47	0	0.30	15.9

Table 3: Asymmetries from various contributions for the 6 rings. A contribution of less than 0.05% is listed as 0.

Looking at the additional degree of freedom of the ϕ sectors, Table 4 shows how the asymmetries are distributed in both radius and ϕ sector. Delving into this one sees, for example, that in ring 2, the ep-elastic contribution varies by less than a factor of two between the sectors, while the e-Al elastic background changes a factor of 7, allowing these two be separated. Similarly, in ring 6 there is a striking difference in the variation with ϕ of the ep-inelastic asymmetry compared to the Moller asymmetry. The ϕ sensitivity is easy to understand - the azimuthal defocussing typical of a toroidal field magnet means that the closed sectors favor events with smaller E', thereby supressing elastic events, for example.

4.3 Structures in Radial Distributions

Before showing the results of a complete simultaneous fit to the simulated asymmetries, we discuss here several interesting features of the $f_i A_i$ vs. radius plots (Fig. 11) which are obvious to the keen eye.

1. The first feature is that the peak ep-elastic contribution (red curve) has a maximum at a radius of about 0.725 m, but there is clear structure (a "shoulder") on the contribution around 0.76 m. This is not a statistical fluctuation in the simulation. In fact, the lower radius peak is where the ep-elastic asymmetry is at its maximum within the acceptance (maximum Q^2), whereas the shoulder at higher radius is where the rate of accepted ep-elastic events is maximum. The contribution to the measured asymmetry, which is a function of the asymmetry weighted by the relevant rate×acceptance, therefore has two local maxima.

2. A second feature that might appear curious is the double-peak structure in the ep-inelastic contribution $f_\mathrm{inel} A_\mathrm{inel}$ (green curve), which might seem unphysical. This is not due to structure in the way the inelastic asymmetry varies with radius. The cause is that the individual dilutions f_i are, by definition, constrained to sum to unity at each ring radius. Thus, while both the rate and asymmetry from one process may be increasing monotonically with radius, if there is a peak in the rate of a competing process at a particular radius, the $f_i A_i$ from the first process is suppressed, and can exhibit a "dip". This is what is happening around radius = 0.75 m: there is a rate maximum for the ep-elastics, which

ring #	sector ID	$\frac{\sigma_A}{A}$ (%)	A_m (ppb)	Møller (%)	e-p elastic (%)	e-p inelastic (%)	e-Al elastic (%)	e-Al quasi-elastic (%)	e-Al inelastic (%)	pions (%)
1	0	9.92	-282.1	0.16	81.6	19.1	-1.06	0	0.23	0
1	1	2.55	-278.2	0	71.7	30.7	-3.29	0	0.87	0
1	2	5.04	-50.92	0	85.7	27.5	-14.6	0	1.34	0
2	0	2.30	-412.2	0	42.5	58.1	-2.50	0	1.77	0.10
2	1	1.18	-203.8	0	56.7	48.0	-6.57	0	1.79	0.06
2	2	1.88	-68.51	0	75.2	39.2	-16.3	0	1.87	0
3	0	3.54	-288.7	0.07	38.0	61.3	-3.55	0	1.21	2.94
3	1	1.83	-176.0	0.06	45.1	58.5	-6.39	0	1.41	1.28
3	2	2.94	-60.01	2.19	56.7	49.6	-10.5	0	1.29	0.75
4	0	6.72	-134.4	3.38	41.8	44.3	-5.22	0	0.76	14.9
4	1	3.83	-98.73	4.91	48.3	41.2	-8.02	0	0.82	12.7
4	2	4.40	-33.88	49.7	32.6	20.7	-7.24	0	0.52	3.60
5	0	4.74	-31.86	87.3	5.46	3.77	-0.82	0	0.08	4.24
5	1	2.57	-35.00	88.0	5.95	3.50	-1.17	0	0.08	3.60
5	2	2.29	-34.34	88.6	7.42	3.56	-1.87	0	0.10	2.17
6	0	21.9	-25.09	42.9	11.7	11.3	-2.43	0	0.30	36.2
6	1	11.2	-16.92	53.8	22.4	7.60	-5.97	0	0.27	21.9
6	2	9.91	-11.47	60.8	28.1	8.55	-8.73	0	0.32	10.9

Table 4: Total predicted asymmetry in each radial ring, A_m, and its statistical precision σ_A/A along with the fractional contributions to the measured asymmetries from each relevant process. "0" indicates that the fraction is less than 0.05%. The definitions of each ring in terms of radius and are given in Fig. 4. The three ϕ sectors are defines as follows: "2" corresponds to a 1/28th fraction of the full range of the azimuth that is centered on an open 1/7th sector of the acceptance collimator, while "0" corresponds to the closed sector of the same ϕ width. The "1" corresponds to the sector in between a "0" and a "2".

locally suppresses the relative contribution from the ep-inelastics (*i.e.* a maximum in the denominator of f_{inel}), generating an apparent "double peaking" in the ep-inelastic contribution.

3. A third feature is that the radiative tail of the ep-elastic events (*i.e.* the rate at large radius) rises above about $r = 1$, while there is no corresponding rise for the ep-inelastic process. This is because deep in the radiative tail (recall that the long hydrogen target corresponds to 17% of a radiation length) one can have hard bremsstrahlung in the initial state, which, for elastic events, implies $Q^2 \rightarrow 0$, which then blows up the elastic form factor. However, with inelastic scattering, a hard bremsstrahlung photon does not necessarily imply $Q^2 \rightarrow 0$, so the form factor does not get large.

4. Finally, we note the important point that the three aluminum contributions also show a "dip" in their $f_i A_i$ in the radial region near 1.0 m (ring 5). This is yet another example of the same effect mentioned above: because the rate of detected Moller electrons peaks at this radius, this locally supresses the relative contribution from the processes on Al, *i.e.* gives $f_{\text{Al\_elastic}}$, *etc.* a minumum.

4.4   Simultaneous Fit results

The 18 asymmetries (6 radial rings, each with 3 ϕ sectors) produced in the full simulation, with statistics corresponding to the full beam time request of 344 days, were simultaneously fitted. The fit had 6 free parameters: the asymmetries for Møller, ep-elastic, e-Al elastic and e-p inelastic (3 W bins) scattering with appropriate Q^2 evolution for each. The f_i dilutions were taken from the simulation. The small contributions from quasielastic scattering and inelastic scattering from the Al windows were subtracted before the simulataneous fit.

Processes	Expected A (ppb)	σ_A (ppb)	$\frac{\sigma_A}{|A|}$ (%)
Moller	-35.20	0.64	1.8
ep-elastic	-19.67	1.82	9.2
ep-inelastic (1)	-439.94	80.6	18.3
ep-inelastic (2)	-433.96	38.3	8.8
ep-inelastic (3)	-384.59	91.5	23.8
eAl-elastic	297.27	83.01	27.9

Table 5: *Results of the simultaneous fit to the 18 quartz tile asymmetries. The asymmetries (A_i) in ring 5 and their fitting errors in ppb and in % are shown.*

The results of the fit are shown in Table 5. We see that the desired precision (1.8%) in the Moller asymmetry is achieved. Very similar results are found with a 4-parameter fit (where the ep-inelastics were assumed to have single asymmetry that scales as Q^2, independent of W), with again a 1.8% precision on the Møller asymmetry. The extracted uncertainties are degraded in all the background couplings in the 6-parameter fit due to correlations. We choose this fit as our final result as a very conservative estimate of the systematic errors due to Al and inelastic backgrounds. Table 6 shows the size of each correction as well as systematic error (due to the statistical uncertainties including correlations in the extracted couplings from the fit in Table 5).

The important takeaway message is this: **the radial and azimuthal segmentation of the detector, combined with the toroidal spectrometer optics and the kinematics of the various background processes, will allow us to untangle the Moller asymmetry from those of the dominant background processes, without recourse to other data or theoretical predictions for those background asymmetries**. All that

Process	Correction (%)	Systematic Error (%)
e-p elastic	-6.61	0.38*
e-p inelastic ($W < 1.4$ GeV)	-1.03	0.22
e-p inelastic ($1.4 < W < 2.5$ GeV)	-1.22	0.13
e-p inelastic ($W > 2.5$ GeV)	-1.31	0.36
e-Al elastic	+1.47	0.15*
e-Al other	< 0.10	< 0.10

Table 6: The fractional correction to the Møller asymmetry in Ring 5 and the associated systematic errors due to the extracted fit uncertainties shown in Table 5 are listed. The statistical error in the Møller asymmetry is 1.88%. The rows marked with a * are assumed to have additional external input. The systematic error on the e-p elastic contribution is assigned a fractional error of 5%. The systematic error on the e-Al elastic contribution is assigned as a fractional error of 10% as discussed in Section 3.2.1. The "e-Al other" contributions include quasi-elastic scattering and inelastic scattering from discrete nuclear excited states and the giant dipole resonance.

we require are the cross sections and simple expectations on the leading Q^2 (and, for inelastics, W) dependence of the asymmetries.

Given the individual systematic errors in each correction in Table 6, we have done a preliminary exploration of the correlations between the corrections. We find that the systematic error on the sum of the corrections from the error matrix is of the order of 0.3%, significantly smaller than several of the individual systematic errors. This essentially indicates that the linear combinations of the various components in the corrections in Ring 5 (the main Møller signal) are well constrained in other tiles. Since this requires further study, we just state here that the total systematic error from the corrections due to inelastic scattering are bounded at 0.7% (linear sum of the three components), but that they are likely to be reduced by about a factor of two after further study.

In the future, other data can further constrain the fit. The anticipated measurement of the proton's weak charge from the Qweak experiment will likely result in a reduction in the systematic error in the e-p elastic correction by a factor of two. Qweak is also analyzing inelastic asymmetry data at W's above the Δ taken during special high beam-energy runs which might allow further constraints on the e-p inelastic couplings in the various W ranges.

We are continuing to investigate further optimization of the fitting algorithm. One avenue is to exploit the planned finer ϕ binning of the detector array in the main Moller signal ring (ring 5). We plan on this ring being segmented by another factor of 3 compared to the other rings – this is to divide the high rates in this ring amongst more PMTs. The present fit results simply sum over this finer segmentation, but there may be additional leverage on extracting the backgrounds if we treat the sub-sectors as individual meaurements in the fit. Also, we plan on studying adjustments to the boundaries between individual rings and ϕ sectors to improve the breaking of correlations betweeen the various asymmetry components.

5   Other Backgrounds

While this report focuses on the primary irreducible electron backgrounds from elastic and inelastic scattering from protons and Al nuclei, the collaboration continues to investigate and improve our understanding of the sub-dominant backgrounds, (the second and third categories itemized in Sec. 1.2). Preliminary esti-

mates for all of these components indicate that they are all of the order of, or much smaller than, the ultimate statistical error for the Møller asymmetry measurement. We briefly discuss them in the following.

We expect a small flux of pions, predominantly from photoproduction and electroproduction, in the hydrogen target. We have run Monte Carlo simulations with representations of the MOLLER magnetic fields and collimation using a pion generator based on the Wiser parameterization [25] for direct photoproduction and using the equivalent photon approximation for electroproduction. We find the rate in the Møller ring to be of the order of 0.06%. The parity-violating asymmetry in real photoproduction should be of the order of the hadronic parity-violation parameter f_π, which is experimentally known to be less than 10^{-7}.

We estimate that the rate above is 60% of the total pion rate, with the rest coming from electroproduction. We estimate that the average Q^2 for the latter process is 0.04 GeV^2 and that therefore the parity-violating asymmetry for these pions will be of the order of 4 ppm. Combining all these factors, one can see that the correction in the Møller ring will be of the order of 1 ppb or about 3%. This is the basis of the estimates shown in the last column of Table 2.

Decays of hyperons produced in the hydrogen target require special treatment. Estimates show that the acceptance in the Møller ring is a fractional rate below 10^{-9}. Nevertheless, the analyzing power (polarization transfer from the primary beam electron) could be very significant and we are in the process of carrying out more careful calculations. More importantly, this is the primary reason why we plan to directly measure the pion asymmetry during physics data collection by monitoring the flux of charged particles downstream of the Møller ring and shielding. We estimate that we will measure this asymmetry (nominally expected to be around 1 ppm) to an uncertainty of 0.1 ppm or about 10%.

Finally, we just mention here that Monte Carlo simulations of the full geometry of the collimators, associated shielding, and the quartz detector mechanical structure including light guides are being carried out. In parallel, test beam measurements of the signal efficiency of prototype quartz detectors and background response of the light guide geometry are ongoing. These studies will ultimately lead to an optimization of the geometry of the apparatus so that all other sources of backgrounds and the associated corrections are smaller than the ones discussed in this report.

6   Summary

We summarize the discussion of Aluminum and inelastic backgrounds that have been discussed in previous sections.

6.1   Aluminum Windows

As discussed in detail in Sec. 3.1, there are two major suppression factors in the background correction from the Al target end windows in MOLLER compared to Qweak. The first is that there is more than four times more hydrogen in the MOLLER target for the same window thickness. The second is that the spectrometer focuses scattered electron energy (optimized for the Møller electrons of interest) that are far in momentum from the elastically scattered electrons from target nucleons and nuclei. A full analysis yields that the net correction from elastic scattering from Al nuclei is of order 1.5% in contrast to the Qweak correction of 28%. The accepted q range cuts off at 1 fm^{-1}, well below the first diffraction minimum.

For MOLLER kinematics, we find that quasi-elastic scattering from Al nuclei is highly suppressed and that the correction in the Møller ring is of the order of 0.005%. Even accounting for a signficant enhancement of the parity-violating asymmetry due to final-state interactions would leave this corrections close to negligible. Likewise for inelastic scattering from nuclear excited levels is expected to be smaller than 3% of the total Al rate at Qweak kinematics.

Finally, it is worth mentioning that we will carry out a comprehensive study of trace impurities in the

window material in the future. Should any of these nuclides prove problematic, or if any or the above-mentioned assumptions about inelastic or quasi-elastic scattering become a concern after further study, the collaboration will explore new alloys with signfiicantly lower Z such as ^{7}Be, which would make these backgrounds significantly smaller.

6.2 Inelastic Scattering

A key feature of the MOLLER apparatus is the rich kinematic structure in the detector plane due to the spectrometer optics that provides us with the opportunity to independently extract the weak neutral current vector couplings from various semi-leptonic processes using a simultaneous fit to the measured parity-violating asymmetries in several categories of quartz detector channels. We have discussed results of a fit where the weak charge of the electron (our primary signal), proton and ^{27}Al would be extracted, along with the couplings for inelastic electron-proton scattering in 3 different W ranges: the Δ, other resonances, and continuum.

With the assumption that the parity-violating asymmetry is linearly proportional to Q^2 but is otherwise constant in each W range, we find that the systematic error from the coupling uncertainties are modest and that the total systematic error from inelastic scattering is bounded at 0.7%. We emphasize here again that this estimate is based on using only what is measured in the MOLLER apparatus, and using conservative assumptions on possible correlations. In the future, it is anticipated that further theoretical input, improved optimization of the radial and azimuthal detector segmentation, detailed studies of correlations, and input from other experiments can be used to further reduce the systematic uncertainties.

References

[1] J. Benesch *et al.* [MOLLER Collaboration], arXiv:1411.4088 [nucl-ex].

[2] http://hallaweb.jlab.org/12GeV/Moller/scirev2014/

[3] C. J. Horowitz, Phys. Rev. C **89**, 045503 (2014) [arXiv:1401.6898 [nucl-th]].

[4] D. Androic *et al.* [Qweak Collaboration], Phys. Rev. Lett. **111**, 141803 (2013) [arXiv:1307.5275 [nucl-ex]].

[5] C. Maieron, T. W. Donnelly and I. Sick, Phys. Rev. C **65**, 025502 (2002) [arXiv:nucl-th/0109032].

[6] E. Hadjimichael, G. I. Poulis, and T. W. Donnelly, Phys. Rev. C **45**, 2666 (1992).

[7] P. E. Bosted and V. Mamyan, [arXiv:1203.2262 [nucl-th]].

[8] R. Gonzalez-Jimenez, J. A. Caballero, and T. W. Donnelly, Phys. Rev. C **91**, 045502 (2015) [arXiv:1501.04208 [nucl-th]].

[9] T. Stovall, D. Vinciguerra, and M. Bernheim, Nucl. Phys. A **91**, 513 (1967).

[10] S. Agostinelli *et al.* [GEANT4 Collaboration], Nucl. Instrum. Meth. A **506**, 250 (2003).

[11] D. Androic *et al.* [G0 Collaboration], arXiv:1212.1637 [nucl-ex].

[12] D. Wang *et al.* [Jefferson Lab Hall A Collaboration], Phys. Rev. Lett. **111**, no. 8, 082501 (2013) [arXiv:1304.7741 [nucl-ex]].

[13] D. Wang *et al.*, Phys. Rev. C **91**, no. 4, 045506 (2015) [arXiv:1411.3200 [nucl-ex]].

[14] P. L. Anthony *et al.* [SLAC E158 Collaboration], Phys. Rev. Lett. **95**, 081601 (2005) [hep-ex/0504049].

[15] K. Matsui, T. Sato and T.-S. H. Lee, Phys. Rev. C **72**, 025204 (2005) [nucl-th/0504051].

[16] M. Gorchtein, C. J. Horowitz and M. J. Ramsey-Musolf, Phys. Rev. C **84**, 015502 (2011) [arXiv:1102.3910 [nucl-th]].

[17] N. L. Hall, P. G. Blunden, W. Melnitchouk, A. W. Thomas and R. D. Young, Phys. Rev. D **88**, no. 1, 013011 (2013) [arXiv:1304.7877 [nucl-th]].

[18] N. L. Hall, P. G. Blunden, W. Melnitchouk, A. W. Thomas and R. D. Young, Phys. Lett. B **731**, 287 (2014) [Phys. Lett. B **733**, 380 (2014)] [arXiv:1311.3389 [nucl-th]].

[19] P. E. Bosted and M. E. Christy, Phys. Rev. C P**81**:055213 (2010)

[20] D. S. Armstrong *et al.*, arXiv:1202.1255 [physics.ins-det].

[21] N. L. Hall, P. G. Blunden, W. Melnitchouk, A. W. Thomas and R. D. Young, arXiv:1504.03973 [nucl-th]. (accepted in Phys. Lett B).

[22] D. Androic *et al.* [G0 Collaboration], Phys. Rev. Lett. **108**, 122002 (2012) [arXiv:1112.1720 [nucl-ex]].

[23] S. L. Zhu, C. M. Maekawa, B. R. Holstein and M. J. Ramsey-Musolf, Phys. Rev. Lett. **87**, 201802 (2001) [hep-ph/0106216].

[24] D. Androic *et al.* [G0 Collaboration], Phys. Rev. Lett. **108**, 122002 (2012) [arXiv:1112.1720 [nucl-ex]].

[25] D.E. Wiser, Ph.D. Thesis, University of Wisconsin-Madison, 1977.